RESEARCH PAPER

CrossMark

Computational thermodynamics in ferrite content prediction of austenitic stainless steel weldments

Maria Asuncion Valiente Bermejo [1] · Sten Wessman [2]

Abstract

In this paper, four computational approaches using Thermo-Calc and DICTRA have been used to calculate the ferrite content of a set of austenitic stainless steel welds with different solidification modes and ferrite contents. To evaluate the computational approaches, the calculations were compared to the experimental results. It was found that for each solidification mode, there is one computational approach that predicts ferrite with better accuracy. For ferritic-austenitic alloys, the best accuracy is obtained when considering the peritectic model, with deviations of 1.2–1.4% ferrite. In the case of austenitic-ferritic alloys, the solidification analysed through the eutectic approach showed an accuracy of 0.6–1.6% ferrite, whilst in alloys with fully ferritic solidification, starting calculations, not from the liquid state but from fully ferritic below solidus, was the best approach, showing 2.3% ferrite deviation from the experimental measurements. Computational thermodynamics has proved to be a promising tool to explore simulation and calculation of ferrite content phase fractions in welding. However, further investigation is still needed to correlate the real microstructural features with the computational parameter "cell size". The feasibility and accuracy of computational thermodynamics when predicting ferrite in low-heat-input welding processes such as laser welding is also another aspect for additional investigation.

Keywords Computational thermodynamics · Ferrite · Welding · Stainless steels

1 Introduction

It is well known that the ferrite content in stainless steel welds plays an important role for properties such as corrosion resistance, toughness, strength, and weldability. The desired ferrite balance in austenitic stainless steels and weldments varies depending on the intended application [1, 2]. It is preferable to have contents higher than 3–5 FN (Ferrite Number) as an indication of a mixed ferritic-austenitic solidification and

therefore avoid hot cracking associated with fully austenitic solidification. However, the amount of ferrite should not be greater than 10 FN [3, 4], especially when the material is exposed to high temperatures for long periods or when it is exposed to a sequence of thermal cycles as in multi-pass welding, since ferrite is more prone to transform into brittle intermetallic phases than austenite. Alternatively, cryogenic applications normally require lower than 3 FN to comply with toughness requirements. The relevance of ferrite content for weldability, mechanical properties, and corrosion resistance in stainless steels has been a powerful driving force for researchers to work towards the development of measurement methods and predictive tools since the early part of the twentieth century [5].

For ferrite quantification, magnetic methods, metallography, and crystallography are the three methods used. Magnetic methods [6] are based on the ferromagnetic nature of the ferrite phase. They are very well accepted in the industry, as they are quick and non-destructive and can be used on-site. Metallography assesses the ferrite phase on a previously polished and etched surface by point counting [7] or image analysis. Finally, with more sample preparation and more

---

✉ Maria Asuncion Valiente Bermejo
asun.valiente@hv.se

Sten Wessman
sten.wessman@swerim.se

[1] Department of Engineering Science, University West, SE-461 86 Trollhättan, Sweden

[2] Swerim AB, Box 7047, SE-164 07 Kista, Sweden

expensive equipment, it is possible to use EBSD (electron backscatter diffraction) [8, 9] and XRD (X-ray diffraction) to quantify ferrite contents with some limitations for austenitic stainless steels [10–14].

In terms of predictive methods, the WRC-1992 (Welding Research Council) diagram [15] provides a rapid assessment of ferrite and austenite balance in stainless steel weld metals. This approach started with the Schaeffler diagram in 1947 [16], followed by DeLong [12, 17–19], Siewert [20], Kotecki [15, 21, 22], and Balmforth [23]. The ferrite content is estimated by means of a nickel- and a chromium-equivalent calculated by using the composition of the weld metal. With the Cr- and Ni-equivalents, the intersection with an iso-ferrite line is read from the diagram, in the first diagrams as percentage of ferrite, and in modern diagrams as Ferrite Number [FN], which is an indication of the magnetic response of the material.

The development of software and computing technology in the twenty-first century led to ferrite predictive methods based on mathematical regressions such as Valiente's [24], the use of artificial neural networks such as Vasudevan's [25] and Vitek's [26] but also the start of computational thermodynamics [27] to predict ferrite content. Computational thermodynamics provides the possibility to run complex calculations involving multicomponent equilibria, phase transformations, and complex calculations of thermal properties. Nowadays, it is also possible to couple kinetics to thermodynamics and therefore simulate diffusion-controlled reactions in multicomponent alloy systems, such as the solid-state transformation ($\delta \rightarrow \gamma$) that occurs in stainless steel alloys with primary ferritic solidification.

The austenite formation in the above mentioned solid-state transformation has been the object of studies in duplex stainless steel weldments by computational thermodynamics [28–33]. Wessman [33], using a computational module including diffusion (DICTRA) [34], proposed a simplification in the process by modelling a fully ferritic material below solidus and thus avoided including the liquid phase. That approach was verified by Pettersson et al. [35] who via neutron diffraction at elevated temperature and laboratory furnace heat treatments verified the single-phase ferritic region at elevated temperatures in duplex. Additionally, the usefulness of computational thermodynamics for predicting the ferrite content of stainless steels was shown by Wessman [36] using equilibrium thermodynamics to assess isothermal sections of the Fe-rich corner of the Fe-Cr-Ni system and proving a good fit for the WRC-1992 diagram.

The aim of the present paper is to use different computational thermodynamic approaches to simulate the ferrite content of a set of austenitic stainless steel welds with different compositions and hence different solidification modes and ferrite contents. To validate the simulations, the results will be compared and correlated to the experiments. The purpose is to find the computational approach that best fits the modelling of ferrite formation from the liquid phase down to a temperature reflecting the ferrite content at room temperature.

2 Experimental work

2.1 Materials and welding

Specimens were prepared in a pure argon atmosphere using an electric arc remelting furnace, based on the GTAW (gas tungsten arc welding) process and following the ASTM E1306 standard [37]. A DC power source was used to melt the feed materials at 550 A and 30 V for 60 s.

The feed materials used for the specimens' preparation were three grades of solid wires for GTAW, whose different weight combinations produced the intended range of compositions and solidification modes within the austenitic stainless steel family: purely austenitic [A], austenitic-ferritic [AF], ferritic-austenitic [FA], and ferritic [F] solidification modes. The chemical composition of the four representative alloys selected was analysed by OES (optical emission spectroscopy) and is shown in Table 1.

Ferrite measurements were made by using a calibrated Feritscope on the transverse cross-section of the specimens. The central area of the section was considered representative of an as-welded GTAW deposit in terms of cooling rate and therefore was specifically investigated, avoiding the upper surface that was in contact with the inert gas and the lateral and lower areas, in contact with the copper crucible. The central area investigated at each specimen was 60 mm^2 and 60 individual measurements were conducted to obtain a representative average ferrite value.

The cooling rate of these specimens in the electric arc remelting furnace was determined by DAS (dendrite arm spacing) in a previous project [38] as 10 °C/s.

For microstructural characterisation, light optical microscopy (LOM) and scanning electron microscopy (SEM) were used.

2.2 Computational approach

The simulations were carried out using the following computational tools: Thermo-Calc [27] and the TCFE8 database for thermodynamics and the add-on diffusion module DICTRA [34] with the MOBFE3 database containing the atomic mobility of the elements in ferrite and austenite phases. In DICTRA applications, some simplifications were necessary to reduce the number of interaction parameters for the alloys: the number of elements included was restricted to Fe, C, Cr, Ni, and N, and cooling rate was considered linear.

Table 1 Chemical composition of the alloys [wt.%]

	C	Si	Mn	Cr	Ni	Mo	Cu	N	Others (S + P + O)	Fe (rest)
Alloy 1	0.087	0.47	1.65	24.15	12.30	0.13	0.08	0.041	0.035	61.06
Alloy 2	0.090	0.42	1.62	24.06	12.01	0.13	0.07	0.058	0.040	61.50
Alloy 3	0.078	0.48	1.59	21.97	14.85	0.07	0.05	0.058	0.047	60.81
Alloy 4	0.092	0.39	1.65	26.27	9.46	0.17	0.11	0.072	0.068	61.72

Four different set-ups or approaches were considered for the calculations. The first one (a) used Thermo-Calc to calculate ferrite content under equilibrium conditions and the other three involved the use of DICTRA, which are: (b) solidification from the liquid phase with a eutectic reaction and diffusion, (c) solidification from the liquid phase with a peritectic reaction and diffusion, and (d) starting calculations not from liquid but from a fully ferritic material below solidus and diffusion.

Solidification simulations stop at solidus per se; however, in this paper, the approach in set-ups (b) and (c) was to continue simulation until 1000 °C which is well below solidus. The simulation will thus encompass the whole solidification process: the segregation due to the solidification, the sub solidus homogenisation of segregated parts and connected growth, and the decrease of the matrix phases ferrite and austenite. The simulations were terminated at 1000 °C, assuming that no major changes in the matrix phase balance occur below this temperature at a 10 °C/s cooling rate. In these two approaches, the starting point in DICTRA calculations is a cell consisting of liquid phase with a homogeneous distribution of the alloying elements. The cell size is the size of the system analysed and it can be dendrite size, grain size, austenite spacing, or similar.

Therefore, the cell size is a critical parameter in DICTRA. In this investigation, three cell sizes were selected (5 μm, 10 μm, and 20 μm) according to the results obtained in the metallographic inspection of the alloys. It should be observed that the Ferrite Numbers measured were translated to volume fractions using the translation from [36].

3 Results

3.1 Metallographic inspection and measured ferrite content

Results of ferrite measurements are shown in Table 2 together with the solidification modes found by metallographic inspection. Standard deviation in ferrite measurements was found to be between 0.4 FN for [FA] alloys to 3.0 FN for [F] alloy.

Alloys 1 and 2 presented [FA] solidification mode as shown in Fig. 1. Primary dendrites are ferritic, and austenite is formed in the interdendritic locations at the last stage of the solidification. Once solidification is completed, austenite is formed as a result of the solid-state diffusion-controlled transformation ($\delta \rightarrow \gamma$), and it grows towards the centre of the ferritic dendrites resulting in a skeletal morphology. In these specimens, the secondary arm spacing was measured in 30 locations of the central cross-section and it was found to be 16 ± 3 μm.

Alloy 3 revealed [AF] solidification mode as shown in Fig. 2. Austenitic dendrites formed first and a few interdendritic locations show ferrite with vermicular/globular morphology formed at the last stage of the solidification in the grain boundaries. It is commonly referred to as eutectic ferrite because ferrite is formed from the eutectic reaction ($L \rightarrow \delta + \gamma$) with the last liquid to solidify. The Feritscope does not detect such a small amount of ferrite in this specimen and it is only detected by microscopy.

Alloy 4 had [F] solidification mode as shown in Fig. 3, with acicular ferrite morphology and areas of Widmanstätten austenite plates.

3.2 Computational work

Calculations were run for Alloys 1 to 4 according to the four models described previously (equilibrium conditions, eutectic and peritectic reactions from liquid and fully ferritic below solidus).

Cell sizes to be used in the diffusion module (DICTRA) were selected as a result from the experimental measurements of the secondary dendrite arm spacing (SDAS). It was decided to use 20 μm (round number for SDAS), 10 μm (half of SDAS), and 5 μm (quarter of SDAS).

Diagrams showing temperature versus phase fractions were obtained for each alloy, computational model, and cell size. To

Table 2 Ferrite measured (FN) and solidification modes

Alloy	Ferrite measured (FN)—Feritscope	Solidification mode (*)
1	11.5	[FA]
2	12.3	[FA]
3	0, but 1–2% ferrite by image analysis	[AF]
4	36.8	[F]

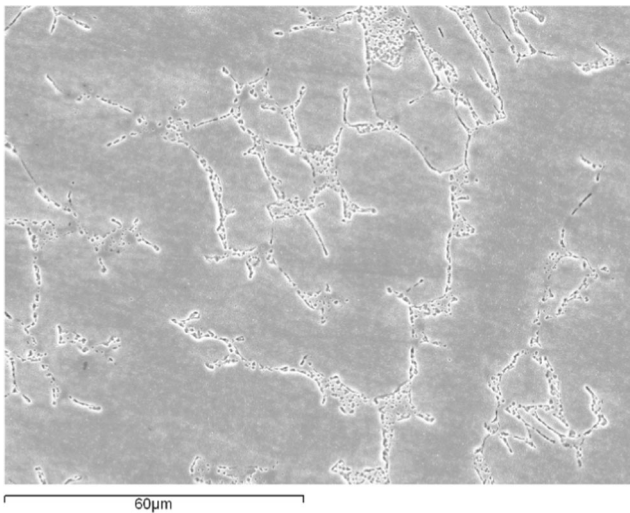(*) *FA*, ferritic-austenitic; *AF*, austenitic-ferritic; *F*, ferritic

Fig. 1 SEM micrograph of alloy 2: skeletal ferrite morphology typical of [FA] solidification mode. Ferrite is revealed bright whilst the austenite matrix is shown in grey shading. Kallings no. 2 was the etching solution

Fig. 3 LOM micrograph of alloy 4: [F] solidification mode showing Widmanstätten austenite plates in the former ferrite grain boundaries and formed in the solid phase after solidification. Austenite is revealed in white colour whilst ferrite is shown in blue and yellow. Ferrofluid EMG 911 was the etching solution

illustrate the evolution of the phases during solidification and cooling within the cell, diagrams showing the phases' fractions versus temperature and distance in the cell were also prepared. A summary of the results is presented below.

Table 3 summarises for each alloy the experimental and calculated ferrite contents obtained according to the different approaches.

3.2.1 [FA] solidification mode, alloys 1 and 2

Figures 4 and 5 illustrate the temperature versus the distribution of the phases' fraction in the cell (10-μm size) comparing the peritectic and eutectic approaches for alloys 1 and 2.
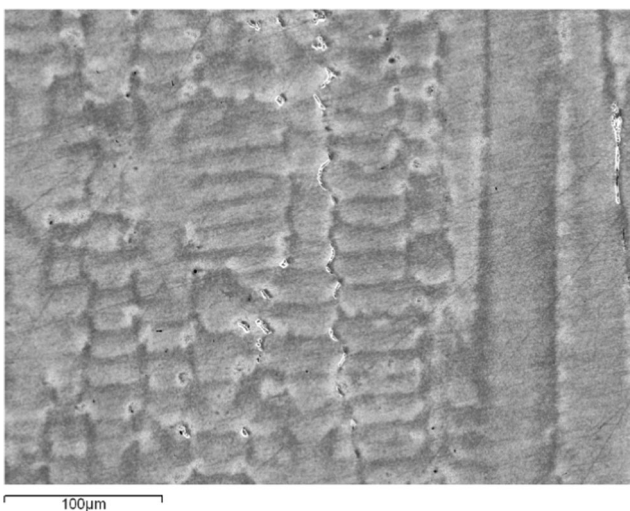

Fig. 2 SEM micrograph of alloy 3: [AF] solidification mode, eutectic ferrite morphology in the primary austenitic dendrite boundaries. Ferrite is revealed bright whilst the austenite matrix is grey. Kallings no. 2 was the etching solution

Both alloys have similar compositions and the same solidification mode (Table 1); therefore, as expected, Figs. 4 and 5 show the same trend. When comparing the peritectic approach versus the eutectic approach in the figures, both approaches show that ferrite solidifies first and at the end of the solidification ferrite occupies around 45–50% of the cell. During cooling, austenite grows in the cell at the expense of ferrite, according to the solid-state diffusion-controlled transformation ($\delta \rightarrow \gamma$). The final ferrite content differs, being the peritectic approach (10–15% of the cell) closer to the experimental values as shown in Table 3 and in Figs. 4 and 5.

3.2.2 [AF] solidification mode, alloy 3

Figure 6 shows the temperature versus the distribution of the phases' fraction in the cell (10-μm size) for alloy 3 comparing peritectic and eutectic approaches. In both peritectic and eutectic, austenite solidifies first and after cooling austenite occupies around 95% of the cell.

3.2.3 [F] solidification mode, alloy 4

Figure 7 illustrates the temperature versus ferrite-phase fraction for alloy 4 comparing equilibrium, experimental, and computational eutectic, peritectic, and ferritic approaches for 5-μm and 10-μm cell sizes.

Figure 8 shows the temperature versus the distribution of the phases' fraction in the cell (10-μm size) for alloy 4 comparing peritectic and eutectic approaches. Both approaches show that ferrite solidifies first and at the end of the solidification ferrite occupies around 80% of the cell. During cooling, austenite grows in the cell at the expense of ferrite, according

Table 3 Summary of ferrite content results

Alloy	Experimental (FN)	Experimental translated to vol.% [28]	Predicted thermo-calc (vol.%)	DICTRA eutectic model (vol.%)			DICTRA peritectic model (vol.%)			DICTRA ferritic model (vol.%)		
				5 μm	10 μm	20 μm	5 μm	10 μm	20 μm	5 μm	10 μm	20 μm
1	11.5	13.5	4.8	18.2	22.0	28.6	8.1	11.3	14.7	–	–	–
2	12.3	14.1	3.6	17.4	21.0	26.7	7.4	10.5	12.7	–	–	–
3	0, but 1–2% by image analysis	0 but 1–2% by image analysis	0	2.6	5.0	6.3	2.8	5.7	6.8	–	–	–
4	36.9	34.0	25.4	38.8	47.2	61.3	21.6	26.6	49.4	36.3	43.5	55.5

to the solid-state diffusion-controlled transformation ($\delta \rightarrow \gamma$) and the final ferrite predicted content differs. However, as shown in Fig. 7 and in Table 3, the computational approach closest to the experimental results is the ferritic model considering a 5-μm cell size.

4 Discussion

In this chapter, the influence of the solidification mode and the cell size on the accuracy of the ferrite content predictions are discussed.

Alloys 1 and 2 show [FA] solidification mode. The composition of these alloys falls into the three-phase area ($L + \delta + \gamma$) of the Fe-Cr-Ni phase diagram and the solidification mechanism proposed in the literature [39–46] is known as "peritectic-eutectic reaction". Solidification starts with ferrite, but before the end of the solidification, some austenite is formed in equilibrium with the ferrite and the last liquid. It is the result of a transition from a peritectic reaction in the Fe-Ni system ($L + \delta \rightarrow \gamma$) to a

eutectic reaction ($L \rightarrow \delta + \gamma$) in the Fe-Cr-Ni system. The composition which establishes the transition between the peritectic to the eutectic under welding conditions is not clear yet. Once solidification is completed, austenite is formed as a result of the solid-state diffusion-controlled transformation ($\delta \rightarrow \gamma$) and it grows towards the inside of the ferritic dendrites, resulting in a skeletal morphology.

For both Alloy 1 and Alloy 2, as shown in Table 3 and Figs. 4 and 5, the peritectic model predicts ferrite content with better accuracy than the eutectic model and most representative cell size in DICTRA was 20 μm, i.e. differences in the range of 1.2–1.4% ferrite were observed between the experimental values and the peritectic model calculation using 20 μm as cell size. As previously mentioned, the composition which establishes the transition between the peritectic to the eutectic reactions under welding conditions is not clear yet, and it is possible that slight differences in compositions, within alloys with [FA] solidification mode, might influence the extent and contribution of the peritectic reaction versus the eutectic reaction.
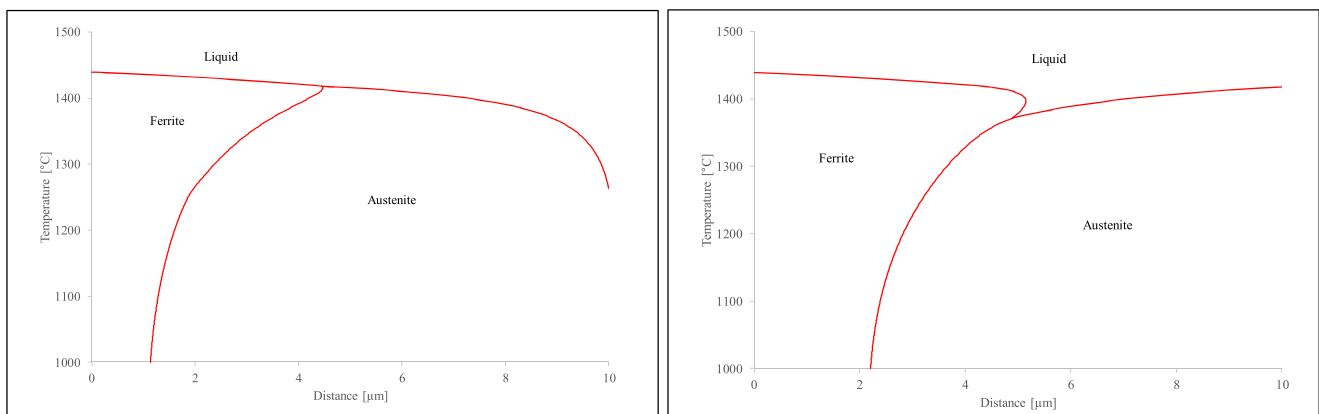

Fig. 4 Left-peritectic approach. Right-eutectic approach. Temperature [°C] vs. phases' fraction distribution in the 10-μm cell for alloy 1, 10 °C/s cooling rate
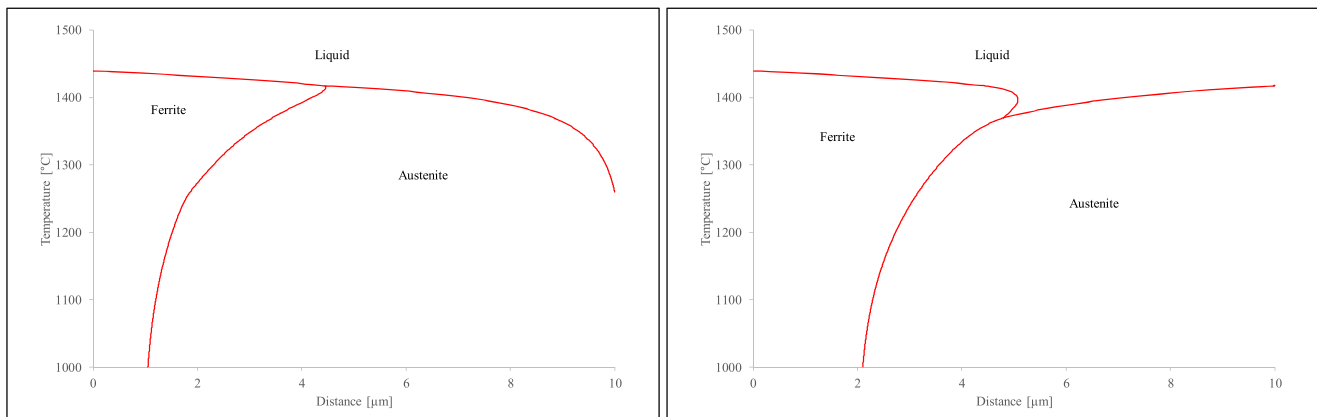
Fig. 5 Left-peritectic approach. Right-eutectic approach. Temperature [°C] vs. phases' fraction distribution in the 10-μm cell for alloy 2, 10 °C/s cooling rate

Alloy 3 solidifies as [AF]. In this alloy, ferrite can be detected by metallographic inspection but in such a small amount (1–2%) that the Feritscope could not detect it. Austenite phase is formed first and ferrite is formed from the last interdendritic liquid which is enriched in Cr due to compositional segregation during austenite solidification. Ferrite formation follows the eutectic reaction $L \rightarrow \delta + \gamma$. In alloy 3, the model that predicts the closest value to the experimental one is the eutectic model using the smallest cell size (5 μm), with an accuracy of 0.6–1.6% ferrite.

Alloy 4 solidifies as [F], fully ferritic. It means that only ferrite phase solidifies from the liquid and ferrite is the only phase just below solidus ($L \rightarrow L + \delta \rightarrow \delta$). Austenite is formed as a result of a solid-state diffusion-controlled reaction. In this case, it was found that the best computational approach was the one that does not consider solidification from the liquid and starts calculations in the solid state as fully ferritic. Therefore, the ferritic model with a 5-μm cell size gives the most accurate calculation, with only 2.3% ferrite deviation from the experimental ferrite for alloy 4. As previously

referred, this is the same approach that was successfully used with duplex and superduplex in previous works. The approach that includes the liquid for Alloy 4 also indicates that neither the peritectic nor the eutectic model give a fully ferritic solidification. This was discussed in ref. [33] and is due to the TCFE database failing to predict this, the likely reason being an underestimation of the nitrogen solubility of the ferrite at elevated temperatures. An effect of this can also be seen in Fig. 7 where the point at which ferrite starts to form is above solidus for the ferritic approach without liquid.

As shown in Figs. 4, 5, 6 and 8, it was possible to predict the evolution of the phases during solidification and cooling within the cell for the peritectic and eutectic approaches. The certainty of these diagrams at temperatures above solidus is not in the scope of this work, and it would need further evaluation by using advanced characterisation techniques such as neutron diffraction at high temperatures. However, the predicted evolution of phases matches the resulting microstructures at room temperature and the extensive literature on solidification modes for austenitic stainless steel welds.
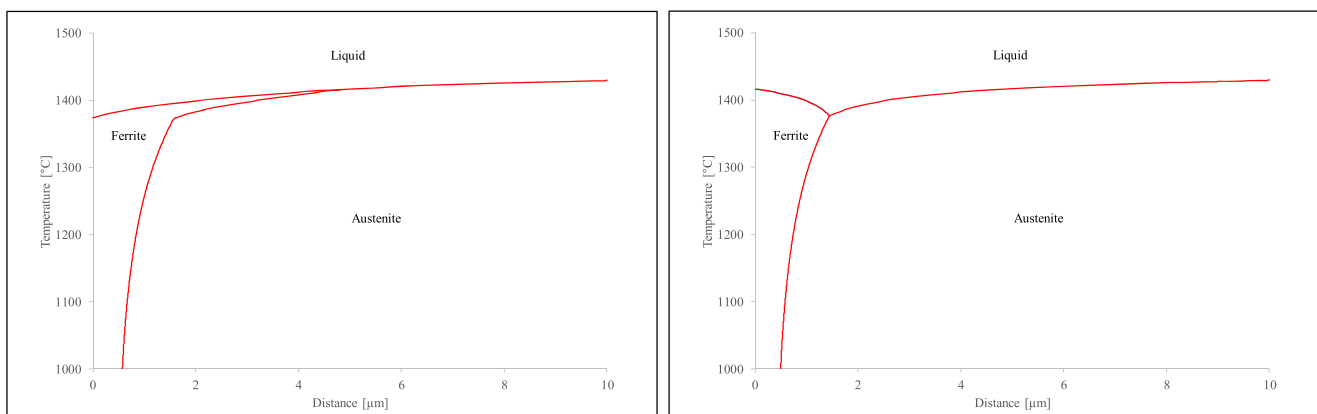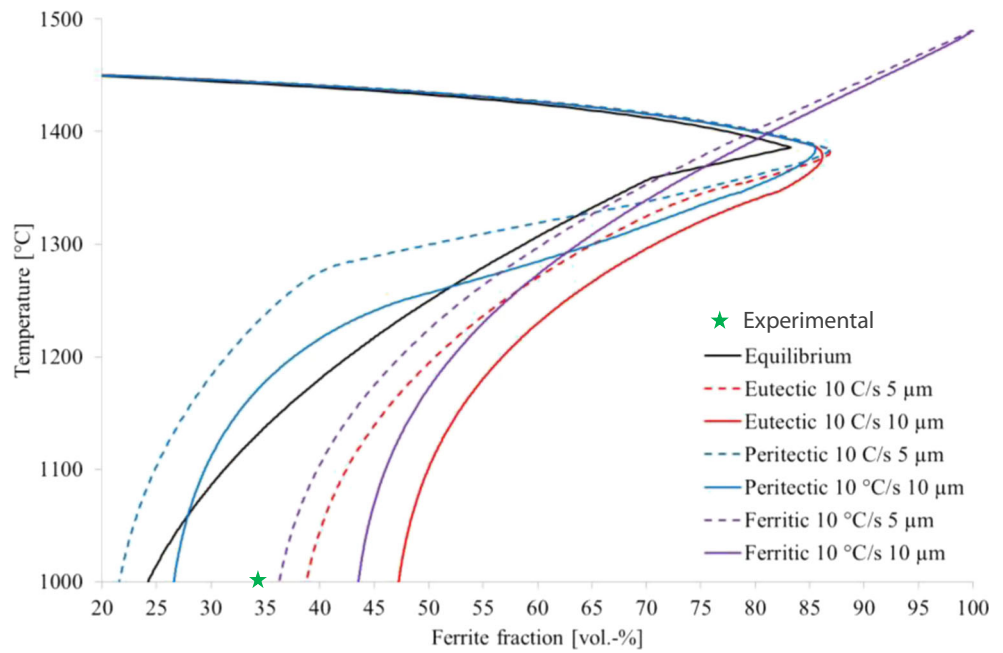

Fig. 6 Left-peritectic approach. Right-eutectic approach. Temperature [°C] vs. phases' fraction distribution in the 10-μm cell for alloy 3, 10 °C/s cooling rate

Fig. 7 Temperature [°C] vs. ferrite fraction [vol.%] for alloy 4, 5- and 10-µm cell sizes, 10 °C/s cooling rate. Equilibrium (by Thermo-Calc), eutectic, peritectic, and ferritic models (by DICTRA)

Despite the uncertainty inherent to the computational methods, such as the limitation in the number of elements for diffusion calculations, the translation of the FN to vol.% or the reliability of databases, it can be concluded that Thermo-Calc and DICTRA provide a good approach to the experimental measurements, which also have their own uncertainty.

In terms of cell size, it has been observed that the larger the cell size, the more ferrite is obtained in DICTRA calculations. It happens systematically in all the models used (eutectic, peritectic, and ferritic). Further investigations to determine the sensitivity of cell size to phase fractions would be necessary. Maybe the fact that calculations are 1D whilst microstructures are 3D could have an influence that would need further investigation.

Computational thermodynamics is a powerful instrument to explore simulation and calculation of phase fractions for different welding conditions. The next aspects that need further investigation are the relationship between the real microstructural features and the "cell size" as key computational parameter. Further work should also be conducted on the feasibility of computational thermodynamics to predict ferrite content in low-heat-input welding of austenitic stainless steels, such as laser beam welding, when cooling rates can be in the range of 10^3–10^5 °C/s.
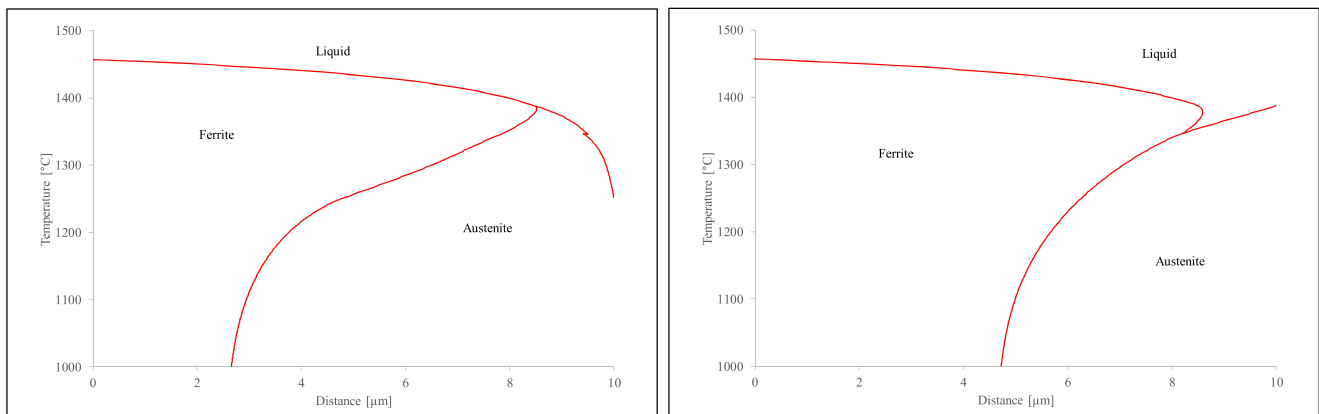

Fig. 8 Left-peritectic approach. Right-eutectic approach. Temperature [°C] vs. phases' fraction distribution in the 10-µm cell for alloy 4, 10 °C/s cooling rate

5 Conclusions

Four computational thermodynamic approaches were considered to calculate ferrite content in austenitic stainless steels welds, one using Thermo-Calc and three approaches involving DICTRA. To evaluate the accuracy of the computational approaches, the calculations were compared to the experimental results.

The computational approach that best simulates the ferrite content in austenitic stainless steels was found to be connected to the solidification mode of the alloy:

– In alloys with fully ferritic solidification mode [F], starting calculations not from liquid but from fully ferritic below solidus and a 5-μm cell size gave the most accurate figure, with 2.3% ferrite deviation from the experimental value.
– For ferritic-austenitic alloys [FA], the peritectic model with a 20-μm cell size showed better accuracy with deviations in the range of 1.2–1.4% ferrite from the measured values.
– In the case of alloys with austenitic-ferritic solidification mode [AF], the eutectic model using a 5-μm cell size gave an accuracy of 0.6–1.6% ferrite.

DICTRA proved to be a useful and accurate tool for estimating the ferrite content in austenitic stainless steel welds experiencing low cooling rates.

References

1. Brouwer G (1978) Ferrite in austentic stainless steel weld metal-advantage or disadvantage?, Philips Welding Reporter, vol 3, pp 16–19
2. Lefebvre J (1993) Guidance on specifications of ferrite in stainless steel weld metal. Welding in the World 31(6):390–406
3. ASME III, Division 1, Subsection NB "Rules for construction of nuclear power plant components", paragraph NB-2433.2 (2005)
4. API recommended practice 582 Welding guidelines for the chemical, oil and gas industries, (2001)
5. Valiente-Bermejo MA (2012) Predictive and measurement methods for delta ferrite determination in stainless steels. Weld J 91(4):113s–121s
6. Cullity BD (1972) Introduction to magnetic materials. Addison-Wesley Publishing, Boston
7. ASTM E562-11 (2011) Standard test method for determining volume fraction by systematic manual point count. ASTM International, West Conshohocken
8. Shrestha SL, Breen AJ, Trimby P, Proust G, Ringer SP, Cairney JM (2014) An automated method of quantifying ferrite microstructures using electron backscatter diffraction (EBSD) data. Ultramicroscopy 137:40–47
9. Zhao H, Wynne BP, Palmiere EJ (2016) A phase quantification method based on EBSD data for a continuosly cooled microalloyed steel. Mater Charact 339–348
10. Stalmasek E (1986) Measurement of ferrite content in austenitic stainless steel weld metal giving internationally reproducible results. WRC Bulletin 318:23–98
11. Lundin CD, Ruprecht W, Zhou G (1999) Ferrite measurement in austenitic and duplex stainless steel castings. Literature review submitted to SFSA/CMC/DOE. Materials Joining Research Group, University of Tennessee, Knoxville, 40p.
12. DeLong WT (1974) Ferrite in austenitic stainless steel weld metal. Weld J 53(7):273s–286s
13. SCRATA (1981) The measurements of delta ferrite in cast austenitic stainless steels, Technical bulletin of the steel castings research and trade association, vol 23, 4 p
14. Bonnet C, Lethuillier P, Roualult P (2000) Comparison between different ways of ferrite measurements in duplex welds and influence on control reliability during construction, Duplex America 2000 Conference, pp 431–442
15. Kotecki DJ, Siewert TA (1992) WRC-1992 Constitution diagram for stainless steel weld metals: a modification of the WRC-1988 diagram. Weld J 71(5):171s–178s
16. Schaeffler AL (1949) Constitution diagram for stainless steel weld metal. Metal Progress 56(11):680–680B
17. DeLong WT (1960) A modified phase diagram for stainless steel weld metals. Met Prog 77(2):99–100B
18. Long CJ, DeLong WT (1973) The ferrite content of austenitic stainless steel weld metal. Weld J 52(7):281s–297s
19. Reid HF, DeLong WT (1973) Making sense out of ferrite requirements in welding stainless steels. Met Prog 6:73–77
20. Siewert TA, McCowan CN, Olson DL (1988) Ferrite number prediction to 100 FN in stainless steel weld metal. Weld J 67(12):289s–298s
21. Kotecki DJ (1997) Ferrite determination in stainless steel welds - advances since 1974. Weld J 76(1):24s–37s
22. Kotecki DJ (1982) Extension of the WRC Ferrite Number system. Weld J 61(11):352s–361s
23. Balmforth MC, Lippold JC (2000) A new ferritic-martensitic stainless steel constitution diagram. Weld J 79(12):339s–345s
24. Valiente Bermejo MA (2012) A mathematical model to predict δ-ferrite content in austenitic stainless steel weld metals. Weld World 56(09–10):48–68
25. Vasudevan M, Murugananth M, Bhaduri AK (2002) Application of Bayesian neural network for modeling and prediction of Ferrite Number in austenitic stainless steel welds. In: Cerjak H (ed) Mathematical Modelling of Weld Phenomena, 6th edn. Maney Publishing, Leeds
26. Vitek JM, David SA, Hinman CR (2003) Improved Ferrite Number prediction model that accounts for cooling rate effects-part 1: model development. Weld J 82(1):10s–17s
27. Sundman B, Jansson B, Andersson J-O (1985) The Thermo-Calc databank system. CALPHAD 9(2):153–190
28. Hertzman S, Roberts W, Lindenmo M (1986) Microstructure and properties of nitrogen alloyed duplex stainless steel after welding treatments, Proc. Duplex Stainless Steel, The Hague, The Netherlands, pp 257–267
29. Sieurin H, Sandström R (2006) Austenite reformation in the heat-affected zone of duplex stainless steel 2205. Mater Sci Eng A 418(1–2):250–256

30. Westin EM, Brolund B, Hertzman S (2008) Weldability aspects of a newly developed duplex stainless steel LDX 2101. Steel Res Int 70(6):473–481

31. Vitek JM, Kozeschnik E, David SA (2001) Simulating the ferrite-to-austenite transformation in stainless steel welds. CALPHAD 25(2):217–230

32. Garzón CM, Ramirez AJ (2006) Growth kinetics of secondary austenite in the welding microstructure of a UNS S32304 duplex stainless steel. Acta Mater 54(12):3321–3331

33. Wessman S, Selleby M (2014) Evaluation of austenite reformation in duplex stainless steel weld metal using computational thermodynamics. Weld World 58:217–224

34. Andersson J-O, Höglund L, Jönsson B, Ågren J (1990) In: Purdy CR (ed) Fundamentals and application of ternary diffusion. Pergamon Press, New York 153 pages

35. Pettersson N, Wessman S, Hertzman S, Studer A (2017) High-temperature phase equilibria of duplex stainless steels assessed with a novel in-situ neutron scattering approach. Metall Mater Trans A 48:1562–1571

36. Wessman S (2013) Evaluation of the WRC 1992 diagram using computational thermodynamics. Welding in the World 57(3):305–313

37. ASTM E1306 (2004) Standard practice for preparation of metal and alloy samples by electric arc remelting for the determination of chemical composition. ASTM International, West Conshohocken

38. Valiente Bermejo MA (2010) Modelització del nivell de ferrita als acers inoxidables austenítics sotmesos a fusió per arc elèctric, PhD Thesis, Universitat de Barcelona, Department of Materials Science and Metallurgical Engineering, ISBN 978-84-693-5713-2

39. Brooks JA (1992) Solidification behavior and cracking susceptibility of austenitic stainless steel welds, Proceedings of the 8th Annual North American Welding Research Conference, Columbus, 19–21 October 1992. Ohio, 14 pages

40. Shankar V, Gill TPS, Mannan SL, Sundaresan S (2003) Solidification cracking in austenitic stainless steel welds. Sadhana 28:359–382

41. Katayama S, Fujimoto T, Matsunawa A (1985) Correlation among solidification process, microstructure, microsegregation and solidification cracking susceptibility in stainless steel weld metals. Trans Jpn Weld Soc 14(1):123–138

42. Inoue H, Koseki T, Ohkita S (1997) Effect of solidification and subsequent transformation on ferrite morphologies in austenitic stainless steel welds. International Institute of Welding, 1996. Doc. IX-1835. 24 pages. Abstract in English of 5 technical papers published at Quarterly Journal of the Japan Welding Society 15(1): 77–87, 88–99, num. 2, p. 281–291, 292–304, 305–313

43. Lippold JC, Kotecki DJ (2005) Welding metallurgy and weldability of stainless steels. Wiley-Interscience, New Jersey ISBN 0-471-47379-0

44. Rajasekhar K, Harendranath CS, Raman R, Kulkarni SD (1997) Microstructural evolution during solidification of austenitic stainless steel weld metals: a color metallographic and electron microprobe analysis study. Mater Charact 38(2):53–65

45. Tosten MH, Morgan MJ (2005) Microstructural study of fusion welds in 304L and 21Cr-6Ni-9Mn stainless steels. Westinghouse Savannah River Company, Aiken ref. TR-2004-00456, 27 pages

46. Kundrat DM, Elliot JF (1988) Phase relationships in the Fe-Cr-Ni system at solidification temperatures. Metall Trans A 19A:899–908